Applied Catalysis B: Environmental 320 (2023) 121948

Contents lists available at ScienceDirect

Applied Catalysis B: Environmental

journal homepage: www.elsevier.com/locate/apcatb

CuNCN derived Cu-based/CxNy catalysts for highly selective CO_2 electroreduction to hydrocarbons

Honglin Li [a,1], Shoufu Cao [b,1], Hongman Sun [a,1], Yonglian Lu [a], Ying Zhang [a], Xiaoqing Lu [b,*], Jingbin Zeng [a,*], Zifeng Yan [a,*]

[a] State Key Laboratory of Heavy Oil Processing, College of Chemistry and Chemical Engineering, China University of Petroleum (East China), Qingdao 266580, PR China
[b] School of Materials Science and Engineering, China University of Petroleum (East China), Qingdao 266580, PR China

ARTICLE INFO

Keywords:
Copper
Copper nitride
CuNCN
CO_2 electrochemical reduction reaction
Hydrocarbons selectivity

ABSTRACT

Copper (Cu) has been proved as an efficient catalyst in carbon dioxide electrochemical reduction reaction (CO_2RR) towards hydrocarbons, but still suffers from low selectivity and poor stability. Herein, Cu-based/CxNy catalysts were fabricated by facile pyrolysis of CuNCN in sealed quartz tubes. It is found that CuNCN pyrolyzed at 300 °C (CuNCN-300) exhibits a high C_2H_4 Faradaic efficiency of 48.5% at 500 mA cm^{-2}. However, increasing the pyrolysis temperature above 400 °C gives rise to CH_4 being the predominant product and CuNCN-500 achieves CH_4 Faradaic efficiencies of 66.3% at 300 mA cm^{-2}. Combining experimental and DFT calculation results, Cu_3N plays a crucial role in the formation of C_2H_4, while tri-s-triazine units in CuNCN-500 reduce the barrier of *CO hydrogenation to *CHO and retard C-C coupling on Cu surface. These findings mark the significance of precise tailoring of the synergistic effect between g-C_3N_4 and different Cu species for achieving the desired selectivity during CO_2RR.

1. Introduction

The anthropogenic CO_2 emission has undergone extraordinary increases primarily because of the combustion of fossil fuels [1,2]. Electrochemical CO_2 reduction reaction (CO_2RR) powered by sustainable energy could not only mitigate the risk associated with extensive CO_2 emissions by converting it to value-added fuels and chemicals [3], but also provide an efficient way to store intermittent energy in the form of chemical bonds [4]. Among various metal catalysts utilized in CO_2RR, Cu draws intensive attention due to its moderate binding energy to intermediates ΔE_bCO^* and ΔE_bH^* leading to the high selectivity of hydrocarbons and oxygenates, such as CH_4, C_2H_4, and C_2H_5OH [5–7]. However, it is difficult to obtain high Faradaic efficiency and long-term stability for specific hydrocarbons using Cu as the single active site due to the diversity of products and complex reaction pathways in CO_2RR [8].

Introducing the promoters or second active site into Cu-based catalysts is regarded as one of the promising alternatives to increase the selectivity or reaction rate during CO_2RR [9,10]. For example, the introduction of Ag and Au motivates the C-C coupling ability of copper by efficient CO spillover [11–13]. The ligand stabilized metal oxide clusters on the copper surface promote the CO_2 methanation by adsorbed hydrogen donation from clusters to copper active sites [14]. In addition, the N-containing molecules could also act as promoters to enhance the selectivity and stability of Cu-based catalysts [15]. The amino acid-modified copper electrodes exhibited better hydrocarbons selectivity and the theoretical calculations suggest that the interaction of *CHO and NH^{3+} contributes to the higher hydrocarbons selectivity [16]. N-arylpyridinium-derived film can improve the selectivity of C_2H_4 to 72% by enhancing stabilization of 'top-bound' CO intermediate [17]. The modification of Cu catalysts with N-containing organic polymers could also obtain higher C_{2+} selectivity and reaction rate [18]. NxC environment could activate CO_2 molecules through the specific N-CO_2 interaction and subsequently enhance the C_{2+} selectivity and catalytic stability [19]. In particular, the Cu_3N maintained superior C_2H_4 selectivity in CO_2RR by preserving the Cu(I) in Cu_3N [20–22]. However, post-modification of Cu-based CO_2RR catalysts with polymer is difficult to scale up, and organic molecules modification is usually costly and has poor stability [23]. It is essential to develop more convenient routes to prepare efficient CO_2RR catalysts.

* Corresponding authors.
E-mail addresses: luxq@upc.edu.cn (X. Lu), zengjb@upc.edu.cn (J. Zeng), zfyancat@upc.edu.cn (Z. Yan).
[1] H. Li, S. Cao and H. Sun contributed equally to this work.

https://doi.org/10.1016/j.apcatb.2022.121948
Received 8 May 2022; Received in revised form 18 August 2022; Accepted 3 September 2022
Available online 7 September 2022

A more convenient and effective route is to deposit Cu or Cu_2O nanoparticles on the surface of stable supports, such as carbon black [24], N-doped grapheme [25], g-C_3N_4 [26,27], *etc*. The metal-support interaction could improve the stability and change the electronic properties of Cu catalysts [28]. g-C_3N_4 is a semiconductor with unique structure, which is widely used in photocatalysis due to its excellent synergistic effects with metals and metal oxides [29]. It has been widely used as the promoter to increase the CO selectivity in Au-C_3N_4 and g-C_3N_4/Cu_2O-FeO catalysts [30,31]. Yang et al. reported that the g-C_3N_4 in Au-C_3N_4 catalysts could induce the formation of a negatively charged Au surface, increasing the selectivity of CO in CO_2RR process [32]. Qiao et al. reported that the g-C_3N_4 framework could not only act as a molecular scaffold to uplift copper's D-orbital position toward the Fermi level, but also serve as an additional active center for CO_2RR to enhance the selectivity of CH_4 and C_2H_4 [33,34]. Yi et al. and Fu et al. both reported the synergistic effects between Cu_xO and g-C_3N_4, which contributed to higher selectivity to C_2H_4 (32.2% and 42.2%) than Cu_xO and Cu-C_3N_4 [26,27]. In the above studies, the residual Cu^+ species in oxide-derived Cu catalyst are regarded as the active sites for C_2H_4 production. However, these Cu^+ species are easily reduced during CO_2RR, which will bring controversy to study the intrinsic synergistic effects between g-C_3N_4 and Cu^+ species or metallic Cu [35,36]. Furthermore, a controllable tuning of the states of Cu species on the g-C_3N_4 is lacking, especially the insights into the reaction mechanisms [37]. This absence of knowledge retards the rational design of efficient electrocatalysts utilized in the CO_2RR, and therefore addressing these deficiencies in knowledge is critical.

Herein, in this study, we tune the states of Cu species on g-C_3N_4 supports by controlling the pyrolysis temperature of CuNCN and then demonstrate the crucial role of Cu states and synergistic effects between g-C_3N_4 and Cu^+ species or Cu nanoparticles (NPs) in Cu-based/CxNy CO_2RR catalysts. The CuNCN synthesized by a facile precipitation method would decompose into Cu_3N/CxNy and Cu/CxNy composites at 300 °C and above 400 °C, respectively. The obtained Cu_3N/CxNy (CuNCN-300) achieves the C_2H_4 Faradic efficiency of 48.5% at 500 mA cm^{-2}, while CuNCN-500 and CuNCN-600 achieve CH_4 Faradaic efficiency of 66.3% and 66.2% at 300 mA cm^{-2} in a flow-cell with 1 M KOH as electrolyte, respectively. CuNCN-500 and CuNCN-600 could also achieve CH_4 selectivity of 66.2% and 68.7% in 1 M $KHCO_3$, showing superior resistance to the pH change of electrolyte. According to DFT calculations and experimental results, Cu_3N with superior dispersion in CuNCN-300 promotes the selectivity of C_2H_4 in the flow-cell, and tri-s-triazine structures (g-C_3N_4 fragments) in CxNy enhance the hydrogenation of *CO to *CHO on Cu surface, which is the key step for CH_4 formation.

2. Experimental section

2.1. Chemicals

Cuprous chloride (CuCl) and ammonium hydroxide solution ($NH_3 \cdot H_2O$) were purchased from Sinopharm Chemical Reagent Co. Ltd. Potassium hydroxide (KOH ACS), potassium bicarbonate ($KHCO_3$, 99.99%) and polytetrafluoroethylene preparation (PTFE, 60 wt% dispersion in H_2O) were purchased from Shanghai Aladdin Bio-Chem Technology Co. Ltd. Cyanamide (H_2NCN, 50% in H_2O) was purchased from Shanghai Macklin Biochemical Co. Ltd. Gas diffusion layer (GDL, YLS-30 T) was purchased from Fuel Cell Store. All chemicals were used without further purification. Deionized water was used in all the experimental processes.

2.2. Preparation of catalysts

A precipitation method with slight modifications was utilized to synthesize the CuNCN [38]. Typically, CuCl (247.5 mg) and $NH_3 \cdot H_2O$ (5 mL) were added into 50 mL of deionized water and stirred for 20 min to form a blue solution. 420 μL of H_2NCN (50% in H_2O) was added to another 50 mL of deionized water to form a homogeneous solution. The obtained H_2NCN solution and CuCl solution were mixed and stirred for 5 min to yield a black suspension of CuNCN. The CuNCN precipitation was obtained after filtration and washed several times with deionized water. After drying at 80 °C in a vacuum oven for 1 h, the CuNCN was sealed in quartz tubes. These sealed quartz tubes with CuNCN were put into Muffle furnaces and pyrolyzed at 300, 400, 500, 600 and 800 °C for 1 h with a heating rate of 1 °C min^{-1}, respectively. The obtained samples were denoted as CuNCN-x (x = 300, 400, 500, 600 and 800), where x represents for the pyrolysis temperature.

100 mg of prepared CuNCN-600 was dispersed in 100 mL of diluted HCl solution (4 wt%) and ultrasonicated for 5 min. The resulting solution was stirred under a flow of oxygen for 48 h. Then, the CuNCN-600-HCl was obtained by filtration, washed four times with deionized water, and dried in a vacuum oven at 80 °C.

100 mg of GO synthesized as previously reported (Supporting Information) [39,40] and 100 mg of CuNCN were dispersed into 50 mL of H_2O, respectively, and then mixed, stirred for 1 h, filtered, and dried in a vacuum oven at 80 °C for 1 h. Finally, the obtained CuNCN/GO compound was calcined in a tube furnace at 600 °C for 1 h under an Ar atmosphere (50 mL min^{-1}) with a heating rate of 1 °C min^{-1}.

2.3. Preparation of gas diffusion electrode (GDE)

The purchased GDL (YLS-30 T) was immersed in 6% PTFE solution for two times to enhance the hydrophobicity of GDL and dried in air. Sequentially, 300 μL of PTFE solution was brushed on the back of GDL and dried in air. Then the GDL was transferred into a tube furnace and calcined at 350 °C for 1 h under a flow of N_2. 3.3 mg of prepared catalysts and 10 μL of Nafion were mixed in 2 mL of isopropanol and ultrasonicated for 20 min. Then 1 mL of mixed solution was sprayed on a GDL surface (2.8 cm × 2.8 cm) with a catalyst loading density of ~ 0.21 mg cm^{-2} and dried in air.

2.4. Characterization

X-ray diffraction (XRD) patterns were recorded on PANalytical X'Pert PRO MPD diffractometer equipped with Cu Kα radiation (0.154 nm) at 40 kV and 30 mA. Field emission scanning electron microscopy (FE-SEM) was conducted on a SEM-JEOL-7900 coupled with energy-dispersive X-ray spectroscopy (SEM-EDX) to examine the morphology and element distribution of samples. Transmission electron microscopy (TEM) and high-resolution TEM (HRTEM) images were obtained by a JEM-2100 F with an accelerating voltage of 200 kV. The high-angle annular dark-field scanning transmission electron microscopy (HAADF-STEM) and energy-dispersive X-ray elemental mapping measurements were carried out on a Tecnai F30 microscope at 300 kV. The Fourier transform infrared (FT-IR) spectra were carried out on a Nicolet 6700 (Thermo scientific) with a MCT detector. X-ray photoelectron spectroscopy (XPS) was recorded by Thermo Scientific ESCALAB 250Xi spectrometer with an Al Kα X-ray source. The Raman spectra were measured using a confocal laser micro Raman spectrometer (LABRAM-HR, JY Co.). Thermogravimetric and differential scanning calorimetry (TG-DSC) curves were measured by Mettler Toledo TGA/DSC 3^+ system with 10 °C min^{-1} under N_2 flow (50 mL min^{-1}).

2.5. Electrochemical measurements

CO_2RR was conducted in a flow cell, which was typically composed of three compartments: two chambers for electrolytes (catholyte and anolyte) and a compartment for CO_2 delivery (Fig. S1). The CO_2 was passed through the gas chamber on back side of the GDE with a flow rate of 20 mL min^{-1}. The 1 M KOH was used as the catholyte and anolyte separated by ion exchange membrane (Dioxide Materials Grade 60). The flow rates of catholyte and anolyte were 5 mL min^{-1}. A piece of platinum

foil and Hg/HgO electrode were used as counter and reference electrode, respectively. The linear sweep voltammetry (LSV) curves were conducted with the scan rate of 10 mV s^{-1} in both CO_2 and Ar. The electrochemically active surface area (ECSA) was obtained by double-layer capacitance (Cdl) measurements. Cyclic voltammetry (CV) curves were tested at various scan rates from 5 mV s^{-1} to 80 mV s^{-1} in 1 M KOH and the potential window was from − 0.09 V to − 0.19 V (vs. Hg/HgO). All potentials except Fig. S14 and Fig. S17 were converted to the RHE with manual 90% cell resistance (R) correction compensation using $E(vs\ RHE) = E(vs\ Hg/HgO) + 0.059 \times pH + 0.098 - 90\% \times iR$. The pH of 1 M KOH was 13.8 and pH values were always located between 13.8 and 14.0 during CO_2RR tests (Fig. S21), so the changes in pH values can be ignored. When 1 M $KHCO_3$ was used as the electrolyte, the Hg/HgO reference electrode was replaced by a saturated Ag/AgCl electrode, and other operating parameters were the same as the above parameters. All potentials were converted to RHE with manual 90% iR compensation using $E(vs\ RHE) = E(vs\ Ag/AgCl) + 0.059 \times pH + 0.198 - 90\% \times iR$. The pH of CO_2-saturated 1 M $KHCO_3$ was 7. The R in different electrolytes was measured by electrochemical impedance spectroscopy (EIS) under open circuit potentials (Table S1). Nyquist plotting of EIS was conducted at − 0.1 V (vs Hg/HgO) with frequencies ranging from 100 kHz to 0.01 Hz in 1 M KOH, and the amplitude of applied AC voltage was 5 mV.

The gas products were analyzed by an online gas chromatography (Scion 456 C) equipped with both flame ionization detector (FID) with methanizer and thermal conductivity detector (TCD). The liquid products were quantitatively analyzed by ^{1}H NMR (Ascend 400 Bruker) with water suppression, and dimethyl sulfoxide (DMSO) was used as a standard to quantify the liquid products.

The calculation of gas products Faradaic efficiencies uses the following equation:

$$FE \quad \% = \frac{Q_i}{Q_{total}} \times 100 = \frac{P}{RT} \times \frac{vNFV \times 10^{-3}}{I_{total} \times 60} \times 100$$

where FE is the Faradaic efficiency, P is one atmosphere (1.013×10^5 Pa), R is universal constant (8.314 J mol^{-1} K^{-1}), T is room temperature (298.15 K), v is volume concentration of certain gas product, N is the electron transfer number for certain gas product, F is Faradaic constant (96485 C mol^{-1}), V is emission gas flow rate, I_{total} is total steady-state cell current (mA).

The concentration of gas products and liquid products were all calculated by external standard method, and the calibration curves are shown in Fig. S2 and Fig. S3, respectively. The typical online gas chromatography data and ^{1}H NMR data are shown in Fig. S4 and Fig. S5.

2.6. Computational details

All calculations were carried out by spin-polarized density functional theory (DFT) as implemented in Vienna Ab initio Simulation Package (VASP) 6.1.0 [41] with Perdew-Burke-Ernzerhof (PBE) [42] generalized gradient approximation (GGA). The cutoff energy was set as 420 eV after cutoff testing and the k-points were set to be 3 × 3 × 1 for geometry optimization and 11 × 11 × 1 for density of states calculation respectively. The electronic energy and forces were converged to within 10^{-5} eV and 0.02 eV/Å, respectively. The van der Waals interactions were considered by the method of the Grimme (DFT + D3). The effect of water was taken into consideration using VASP implicit solvent model [43].

Changes of Gibbs free energy were calculated by the computational hydrogen electrode (CHE) model [44], in which the reaction: H^+ (aq) + e^- = 1/2 H_2 (g) is equilibrated at 0 V vs the reversible hydrogen electrode at all pH values. The change of Gibbs free energy (ΔG) for each elementary step was defined as follows,

$$\Delta G = \Delta E + \Delta E_{ZPE} - T\Delta S + \Delta G_U + \Delta G_{pH}$$

where ΔE is the reaction energy, ΔE_{ZPE} and ΔS are the zero-point energy (ZPE) and the entropy difference between the products and the reactants at room temperature (T = 298.15 K), respectively. ΔG_U is the contribution of the applied electrode potential (U) to ΔG, and here is set as 0 V. The ΔG_{pH} represents the free energy contribution due to the variations in H concentration, and in this work the contribution of pH was excluded from consideration.

The primitive cell of Cu_3N was obtained from Material Project [45] and then the surface of (100) was cleaved based on the most exposed surface in the experiment and 3 × 3 supercell was used and the lattice parameter was optimized to be 11.44 × 11.44 Å. The tri-s-triazine structures of g-C_3N_4 were used as the support in DFT calculations and the lattice parameter was optimized to be 14.27 × 14.27 Å. A Cu cluster containing 14 Cu atoms was adopted and anchored at the hole site of g-C_3N_4. The Cu-C model was also studied to explore the supporting effect of Cu cluster. Besides, Cu (111) surface was used for comparison, which has a lattice parameter of 10.22 × 10.22 Å.

3. Results and discussion

3.1. Characterizations of catalysts

The CuNCN, which was synthesized by a facile precipitation method using ammonia solution as the precipitant, was decomposed into Cu_3N or Cu NPs supported on CxNy at different temperatures. The obtained composites are denoted as CuNCN-x, where x is the decomposition temperature (Fig. 1a). The crystal phase transformation in the CuNCN is firstly investigated by the XRD measurement as shown in Fig. 1b. XRD pattern of CuNCN can be well indexed to the previous literature reports (Fig. S6a) [38]. Cu atoms in CuNCN transform into Cu_3N and Cu NPs as the temperature raised to 300 °C and 500 °C, respectively, while CuNCN-400 is the mixture of Cu and Cu_3N (Fig. 1b). CuNCN-x (x = 300, 400, 500 and 600) show additional peaks at 2 theta = 27.8°, which is assigned to the (002) crystal plane of g-C_3N_4 (JCPDS 87–1526) indicating that CxNy in CuNCN-x (x = 300, 400, 500 and 600) contains g-C_3N_4 [46,47]. However, this peak disappears in both CuNCN/GO-600 and CuNCN-800 and only Cu phase can be observed implying the decomposition of g-C_3N_4 (Fig. S6b, c). In addition, the XRD result of CuNCN-600-HCl indicates that the Cu NPs in CuNCN-600 are dissolved in diluted HCl solution (Fig. S6d).

FE-SEM characterization images show that the CuNCN consists of 200–300 nm flower-shaped nanoparticles and the protrusions of nanoparticles become thinner and curly for CuNCN-x (x = 300, 400, 500 and 600) due to the pyrolysis of CuNCN at high temperature (Fig. S7a-e), which is confirmed by TEM images (Fig. 1c-f). The HRTEM images of CuNCN-300 and CuNCN-400 (Fig. 1g, h) show that the lattice fringes are 0.38 nm, 0.22 nm and 0.20 nm corresponding to Cu_3N (100), Cu_3N (111) and Cu (111) plane, respectively. This is consistent with the XRD results (Fig. 1b). The HAADF-STEM images of CuNCN-300, CuNCN-500 and CuNCN-600 (Fig. S8, Fig. 1i) were conducted and the elemental mappings show the uniform distributions of Cu, C, and N species. The CuNCN is decomposed into the composites of Cu NPs (20–30 nm) and N-doped graphene in CuNCN-800 (Fig. S7h, i), which agrees well with the literature [38]. CuNCN/600-GO is composed by Cu NPs (200–300 nm) and reduced graphene oxide (RGO) (Fig. S7f), and the TEM and HRTEM images (Fig. S9) are consistent with the SEM results. The SEM and TEM results of CuNCN/GO-600 indicate the CuNCN/GO composites transform into Cu NPs located at RGO surface, and this result is further confirmed by the thermogravimetric (TG) curve of CuNCN under N_2 flow (Fig. S10). Therefore, pyrolyzing CuNCN in a sealed glass tube is more favorable for the dispersion of Cu NPs due to the presence of CxNy.

The CxNy structures of CuNCN-x (x = 300, 400, 500 and 600) and CuNCN were confirmed by FT-IR spectroscopy (Fig. 2a, Fig. S11). The FT-IR spectrum of CuNCN shows the asymmetric stretching mode (νs) of the NCN matrix at 2040 cm^{-1}, which gradually decreased in CuNCN-x

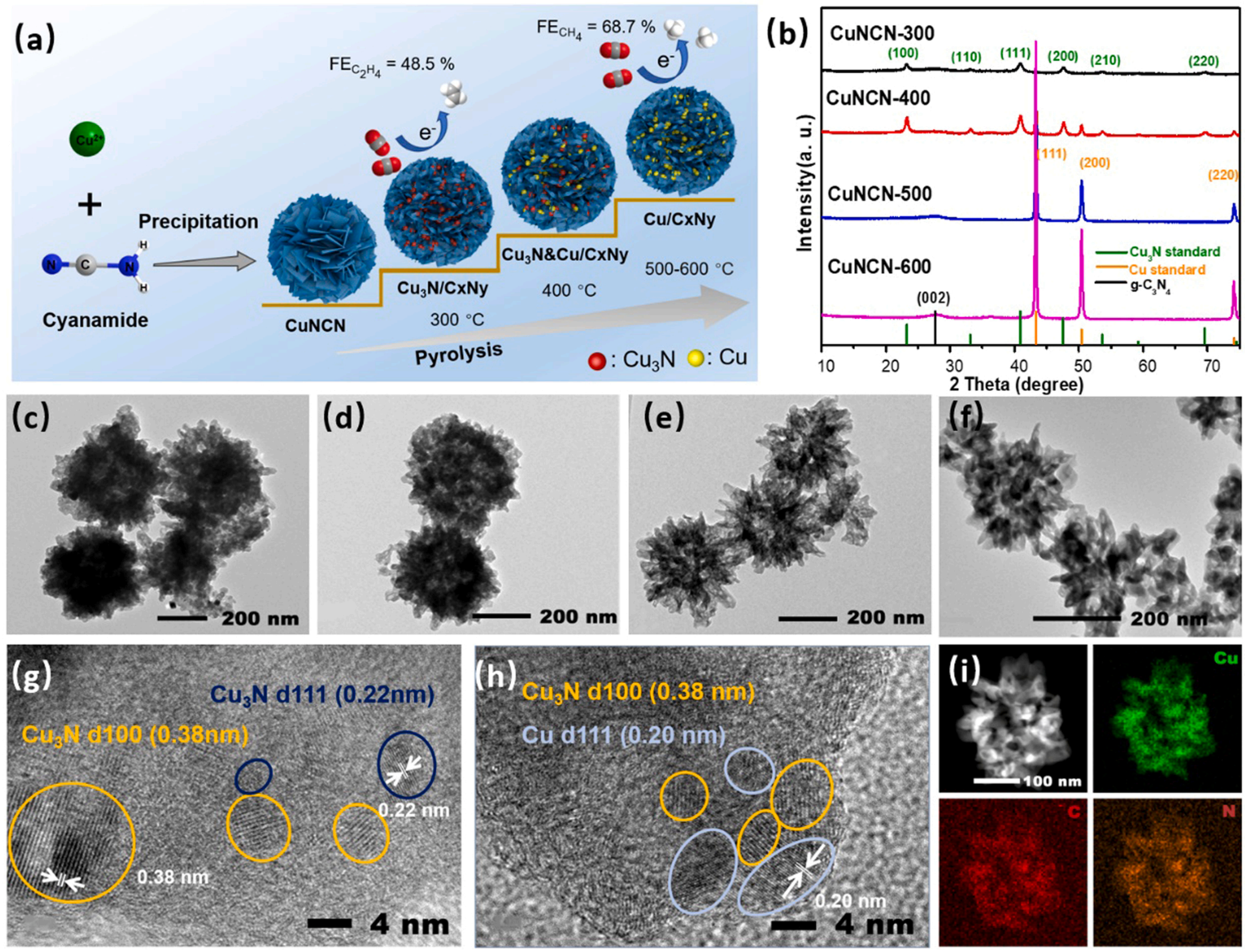

Fig. 1. (a) The schematic illustration of synthesis of CuNCN and preparation of Cu-based/CxNy by CuNCN pyrolysis. (b) XRD patterns and (c)-(f) TEM images of CuNCN-x (x = 300, 400, 500, and 600). (g)-(h) HRTEM of CuNCN-300 and CuNCN-400. (i) HAADF-STEM and elemental mappings of CuNCN-600.

(x = 300, 400, 500 and 600) indicating the decomposition of CuNCN [48]. The IR bands ranging from 1200 to 1600 cm^{-1} can be observed in the CuNCN-x (x = 300, 400, 500 and 600), which are attributed to aromatic heterocyclic C-N bands. In addition, the bands at 770–782.9 cm^{-1} of CuNCN-x (x = 300, 400, 500 and 600) are assigned to the breathing mode of triazine units. Generally, the band of triazine units is located at 800–810 cm^{-1} [49]. After removing Cu NPs by HCl (4 wt%), the bands at 770–782.9 cm^{-1} move back to 810 cm^{-1} (Fig. S11b). Thus, the red shift of triazine units in CuNCN-x (x = 300, 400, 500 and 600) is caused by the interaction between Cu and CxNy [50,51]. Moreover, FT-IR spectroscopy of CuNCN-800 and CuNCN/GO-600 indicate no triazine units in them, and the IR bands ranging from 1200 to 1600 cm^{-1} of CuNCN-800 and CuNCN/GO-600 belong to N-doped graphene (Fig. S11c). The ^{13}C MAS NMR spectrum of CuNCN-400 reveals two signals at 155 ppm and 167 ppm (Fig. 2b), and these shift values represent carbon sites in nitrogen-containing aromatic heterocycles. The value at 167 ppm is similar to sp^2-hybridized carbon atoms in the tri-s-triazine ring of some carbon nitride materials [52,53].

X-ray photoelectron spectroscopy (XPS) was performed on CuNCN-x (x = 300, 400, 500, 600 and 800) and CuNCN/GO-600 to identify the valence states and chemical compositions (Fig. 2c, d and Fig. S12). The N 1 s spectra of CuNCN-x (x = 300 and 400) can be fitted into 3 peaks centering at 397.6, 398.6 and 399.3 eV. The peak at 397.6 eV is attributed to nitrogen atoms in Cu_3N [20]. The peaks at 398.6 and 399.3 eV are corresponded to sp^2 hybridized aromatic N atoms (C=N-C) and tertiary N atoms (N-(C) $_3$) in $g-C_3N_4$, respectively [30,54]. Moreover, the signals of tertiary N atoms (399.3 eV) are quite weak in CuNCN-x (x = 300, 400, 500 and 600), indicating the lower degree of polymerization of nitrogen-containing aromatic heterocycles. The additional peak at 398.3 eV for CuNCN-500 and CuNCN-600 is ascribed to pyridinic N, implying that the tri-s-triazine units are partially decomposed. The N 1 s XPS spectra for CuNCN/GO-600 and CuNCN-800 exhibit four peaks centering at 398.3, 400.5, 402.2 and 404.4 eV, which are assigned to the pyridinic, pyrrolic, graphitic and oxidized nitrogen atoms, respectively (Fig. S12c) [55–57]. The C 1 s XPS spectra for CuNCN-x (x = 300, 400, 500 and 600) contain three components locating at 284.6, 287.3 and 290 eV, corresponding to graphic carbon (C−C), N-C=N in $g-C_3N_4$ and π excitation (or O-C-O), respectively (Fig. 2d) [58]. The peak at 284.6 eV for CuNCN-x (x = 300, 400, 500 and 600) gradually increased, indicating that the graphitization of CuNCN-x is enhanced with the increase of pyrolysis temperature. It is consistent with the intensity change of D bands and G bands in the Raman spectrum results (Fig. S13) [59,60]. The three peaks of CuNCN/GO-600 and CuNCN-800 at 284.6, 285.6 and 288 eV correspond to a graphic carbon (C−C), N-sp^2 carbon (N sp^2 C), N-sp^3 carbon (N-sp^3 C), respectively (Fig. S12d) [55,61]. The absence of peaks centering at 398.6 eV in N 1 s and 287.3 eV in C 1 s for CuNCN/GO-600 and CuNCN-800 indicates that the tri-s-triazine units are fully decomposed, which is in agreement with FT-IR results, XRD patterns and TG curve (Fig. S10). Therefore, CuNCN/GO-600 and CuNCN-800 are both composed of Cu NPs and N-doped graphene, but Cu NPs (200–300 nm) in CuNCN/GO-600 are larger than Cu NPs (20 nm) in CuNCN-800.

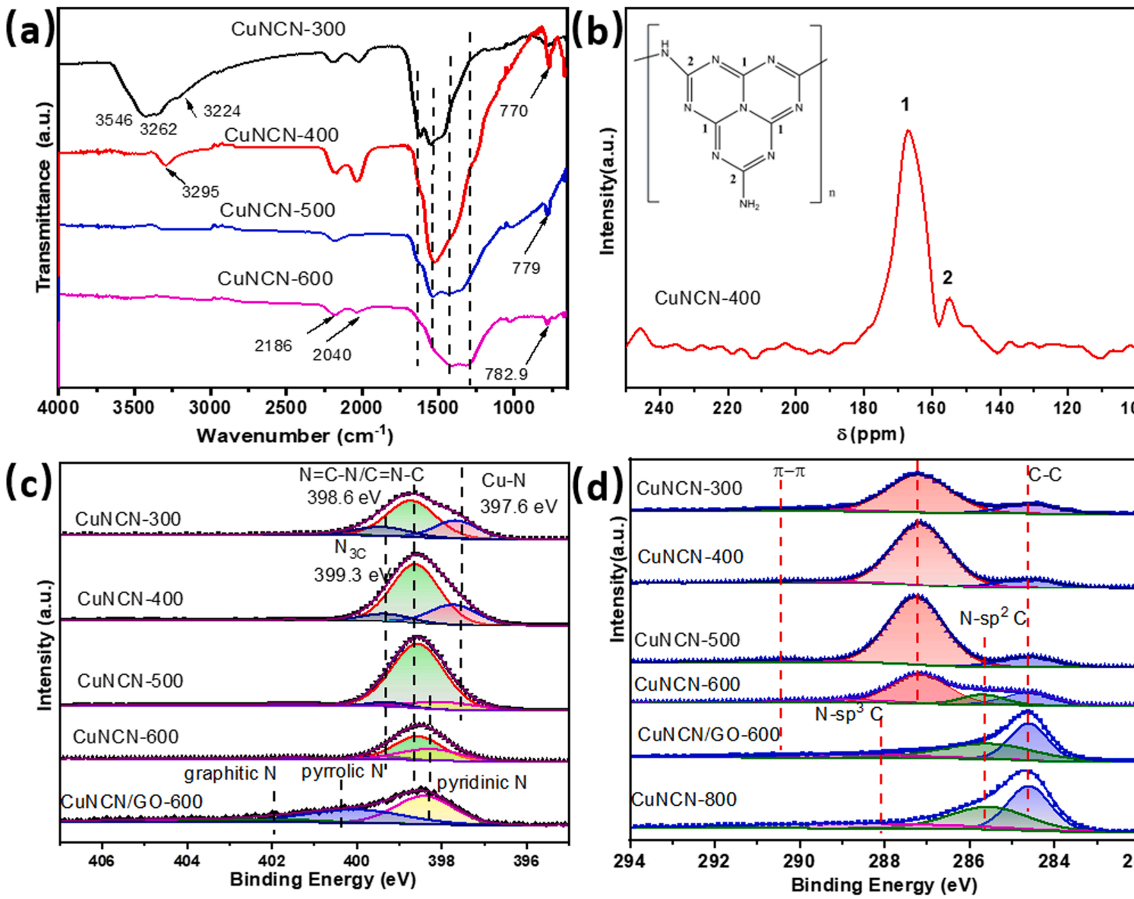

Fig. 2. (a) FT-IR spectra of CuNCN-x (x = 300, 400, 500 and 600). (b) ^{13}C NMR pattern of CuNCN-400. (c) N 1 s XPS and (d) C 1 s XPS spectra of CuNCN-x (x = 300, 400, 500 and 600) and CuNCN/GO-600.

3.2. CO_2RR measurements

The flow-cell could overcome the CO_2 diffusion limitation in CO_2RR tests, and provide more options for electrolytes. Therefore, the flow-cell system could be operated with reasonable energy efficiencies and higher current densities, regarded as the essential factors for commercialization [62]. In our study, the CO_2RR performance of CuNCN-x (x = 300, 400, 500, 600 and 800), CuNCN/GO-600 and CuNCN-600-HCl were firstly evaluated in a flow cell using chronopotentiometry with 1 M KOH as electrolyte. All CO_2RR experiments were carried out at room temperature and atmospheric pressure and all potentials reported (except Fig. S14 and Fig. S17) were transformed into reversible hydrogen electrode (RHE) and with manual 90% iR compensation. The cell resistances of all samples in 1 M KOH were measured by EIS under open circuit potentials (Fig. S15c) and the exact values of cell resistance were given in Table S1. The electrochemically active surface area (ECSA) was obtained by double-layer capacitance measurements (Fig. S14, Fig. 3a and Fig. S15a, b). CuNCN-400 and CuNCN-500 display higher ECSA among CuNCN-x (x = 300, 400, 500, 600 and 800). Moreover, the CuNCN/GO-600 gives highest ECSA and better charge transfer ability because of the addition of GO. The LSV curves for all samples were measured under both CO_2 and Ar atmospheres at 10 mV s^{-1} (Fig. 3b

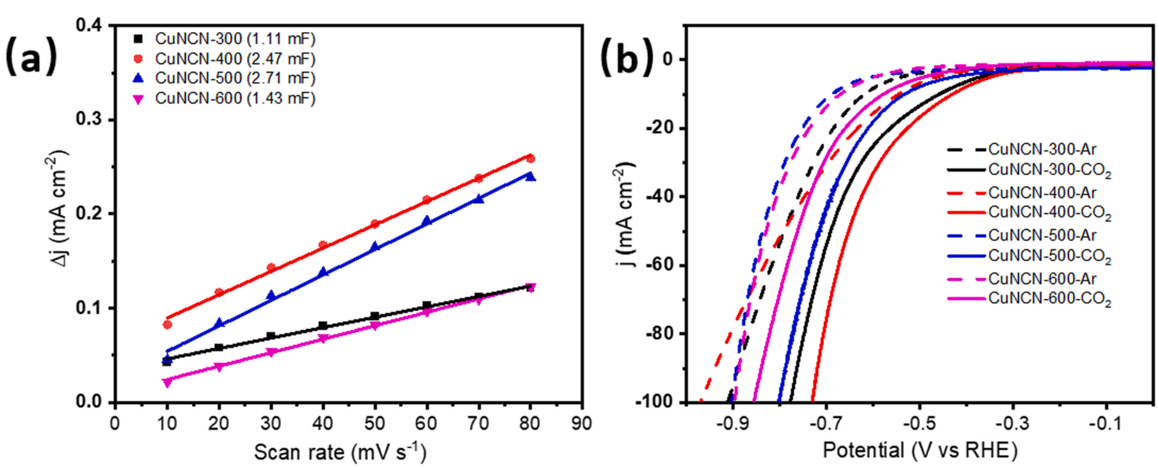

Fig. 3. (a) Double-layer capacitance (Cdl) and (b) LSV curves of CuNCN-x (x = 300, 400, 500, 600) in flow-cell with 1 M KOH as electrolyte.

and Fig. S16c). All these samples (except CuNCN-600-HCl) display larger current densities in CO_2 than those in Ar atmosphere, indicating that the CO_2RR process is priority among these catalysts.

The Faradaic efficiencies for CuNCN-x (x = 300, 400, 500, 600 and 800), CuNCN/GO-600 and CuNCN-600-HCl as the function of current densities are shown in Fig. 4 and Fig. S16a-b. CuNCN-300 achieves the highest Faradaic efficiency of C_2H_4 to 48.5% at 500 mA cm^{-2} and the Faradaic efficiency of CO is also much higher than CuNCN-x (x = 400, 500, 600 and 800). Interestingly, the Faradaic efficiencies of CH_4 for CuNCN-400, CuNCN-500 and CuNCN-600 are 62.8%, 66.3% and 66.2% at 300 mA cm^{-2}, respectively, while the selectivity of CO is much lower than that of CuNCN-300. This indicates that the Cu_3N in CuNCN-300 enhances the selectivity of CO and sequentially promotes the C_2H_4 production. Moreover, the experimental results indicate that Cu_3N in CuNCN-300 shows higher overpotentials for C_2H_4 than that for CH_4 over Cu in CuNCN-500 and CuNCN-600 (Fig. 4 and Fig. S17). Thus, CuNCN-400 shows the similar CO_2RR performance to CuNCN-500 and CuNCN-600, even though the CuNCN-400 both contains Cu_3N and Cu as the activity sites. The Faradaic efficiencies of total liquid products for CuNCN-600 are less than 13% (Fig. S16a), so the liquid products for CuNCN-x (x = 400, 500, 600 and 800) are not considered in this work. CuNCN/GO-600 is mainly composed of Cu NPs and N-doped graphene due to CuNCN would decompose into Cu NPs between 200 and 300 nm and gas in an inert atmosphere. The Faradaic efficiency of CH_4 is 40.9% at 300 mA cm^{-2} over CuNCN/GO-600, which is lower than CuNCN-600, indicating the well dispersed Cu NPs on $g\text{-}C_3N_4$ is the optimal configuration for the generation of CH_4 in this research. In addition, CuNCN-600-HCl exhibits poor CO_2RR activity in this study (Fig. S16b), which means the CxNy shows no activity for CO_2RR and Cu NPs are the active sites for CO_2RR. Therefore, the synergistic effect between Cu NPs and $g\text{-}C_3N_4$ contributes to the highest CH_4 selectivity of CuNCN-600. CuNCN-800 shows 47.9% Faradaic efficiencies for CH_4, which is also lower than

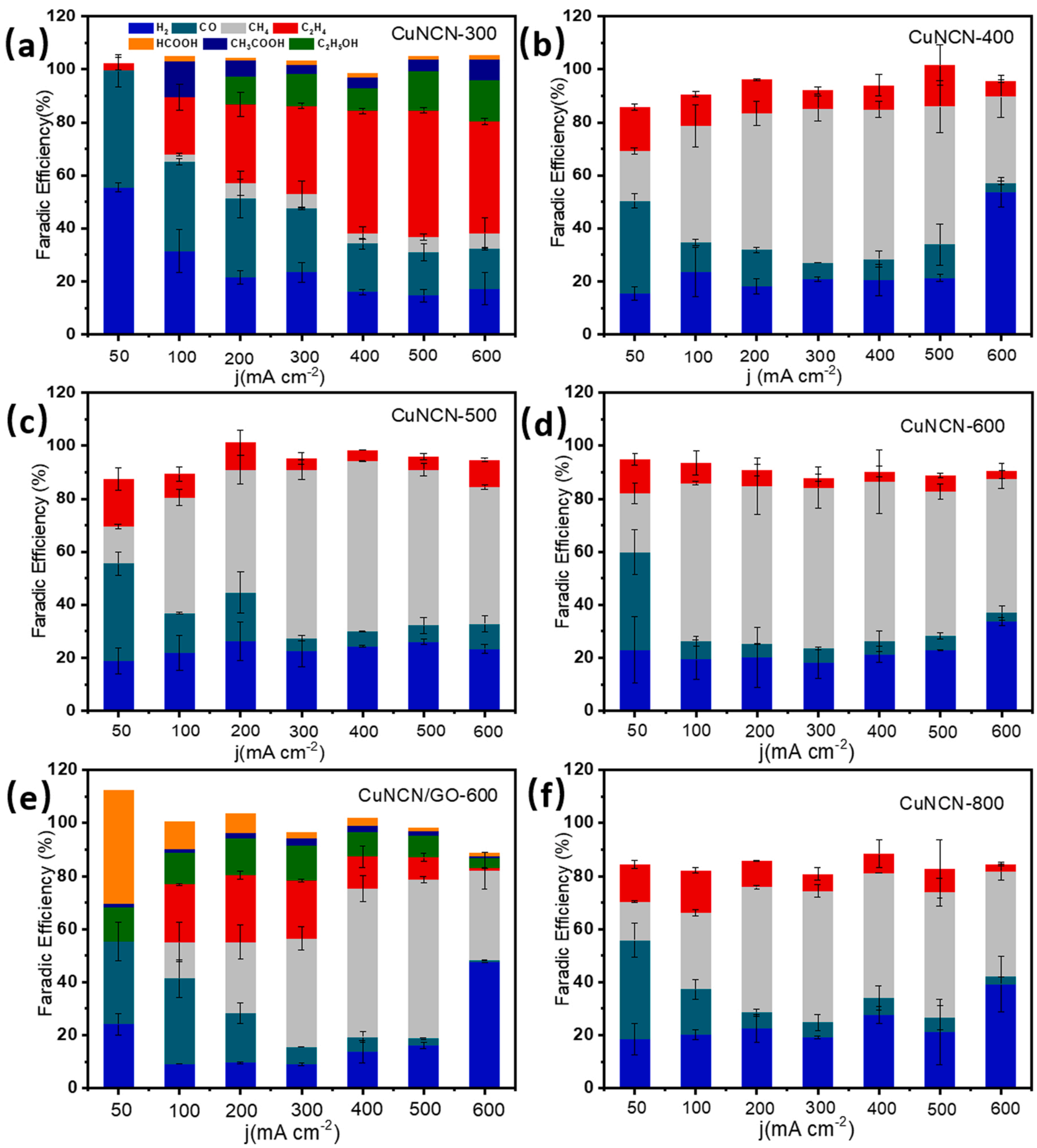

Fig. 4. Faradaic efficiencies of products for (a) CuNCN-300, (b) CuNCN-400, (c) CuNCN-500, (d) CuNCN-600, (e) CuNCN/GO-600 and (f) CuNCN-800 in a flow cell with 1 M KOH as electrolyte.

CuNCN-x (x = 400, 500 and 600) due to the decomposition of g-C_3N_4 at 800 °C. The CO_2RR results indicate the CuNCN-300 and CuNCN-x (x = 400, 500 and 600) show best selectivity for C_2H_4 and CH_4 in 1 M KOH, respectivily. To confirm the catalytic performance of CuNCN-x in neutral electrolyte, the 1 M KOH was replaced by 1 M $KHCO_3$ (Fig. 5 and Fig. S18) during CO_2RR measurements. The CuNCN-500 and CuNCN-600 still maintain 61.4% and 68.7% Faradaic efficiencies for CH_4 and less H_2, while CuNCN-300 still gives the highest selectivity for C_2H_4 among all samples.

3.3. Stability test

The stability of CuNCN-300 and CuNCN-500 was evaluated in a flow-cell at 500 mA cm^{-2} and 300 mA cm^{-2} (Fig. 6), respectively with 1 M KOH as the electrolyte. The KOH as electrolyte maintains lower cell resistance, which is beneficial to reduce heat generation in the flow cell. However, KOH precipitates would be formed on the back of the GDE during long-term test, and we used deionized water to wash the GDE for 3–4 times during the stability test. It is found that CuNCN-300 and CuNCN-500 could achieve high Faradaic efficiency of 41.5% and 61.2% to C_2H_4 and CH_4 after 6 h, respectively. The Faradaic efficiency of C_2H_4 over CuNCN-300 gradually decreased, while the Faradaic efficiency of H_2 and CH_4 increased to 23.7% and 18.8% after 6.7 h. SEM images after stability test indicate the CuNCN-300 is cracked and some fragments aggregates. However, the CuNCN-500 still maintains the initial morphology (Fig. S19). SEM-EDS results indicate that the N element in CuNCN-300 is lost after stability test, which might be the reason for the deactivation (Fig. S20).

3.4. DFT calculations

To further investigate the role of CxNy support in the *CO hydrogenation procedure which was the rate-determining step (RDS) for CH_4, DFT calculations were conducted to calculate the free energy of *CO hydrogenation to *CHO procedure. According to the characterization of CuNCN-x (x = 400, 500, 600), the CxNy contains many tri-s-triazine units which belonging to the g-C_3N_4 fragments. Therefore, the tri-s-triazine structures of g-C_3N_4 was adopted as the support for CuNCN-x (x = 400, 500, 600) in DFT calculations. Compared with CuNCN-500 and CuNCN-600, the most special feature of CuNCN-300 is that Cu exists in the form of Cu_3N, evidenced by XRD and XPS. In addition, it is indicated the Cu_3N (100) is the most exposed surface in HRTEM images. Thus, the Cu_3N (100) surface is used to model the structure of CuNCN-300. CuNCN/GO-600 and CuNCN-800 are composed of Cu NPs and N-doped graphene, but the N content is relatively low. To demonstrate the effects of the special electronic structure of g-C_3N_4 on the Cu clusters, we chose the Cu-C model as a comparison to explore the support effect of Cu clusters. Besides, CO_2RR performance is also studied on Cu (111) for comparison. Fig. 7a and Fig. 7c show the adsorption configurations of *CO and *CHO on Cu-C_3N_4, Cu-C, Cu (111) and Cu_3N (100) and the free-energy diagram of *CO hydrogenation to *CHO. According to Fig. 7c, the Gibbs free energy for *CHO formation is 0.29 eV on Cu-C_3N_4, which is much lower than that on Cu (111) and Cu-C. Moreover, the reaction free energy for the hydrogenation of *CO on Cu_3N (111) is 0.37 eV, which is also lower than that in the Cu (111) and Cu-C system. Cu-C structure needs to overcome much larger reaction energy (0.82 eV) than Cu-C_3N_4 (0.29 eV), which is comparable to that on Cu (111). This suggests that the graphene does not seem to be a promoter to the formation of *CHO intermediate, and this result is consistent with the lower hydrocarbons selectivity of CuNCN/GO-600 and CuNCN-800 than that of CuNCN-600. Therefore, Cu-C model was not considered in C-C coupling procedure.

The adsorption configurations of *CHO, *CO and *CHOCO on Cu-C_3N_4, Cu (111) and Cu_3N (100) and the free-energy diagram of *CHO coupling with *CO to *CHOCO were also conducted as shown in Fig. 7b and Fig. 7d. The Cu-C_3N_4 demonstrates the highest free energy of 0.36 eV for *CHO-*CO coupling, while this procedure is most favorable on Cu_3N (100) surface (−0.21 eV). The maximum value for Cu-C_3N_4 in Fig. 7c and Fig. 7d is 0.36 eV, which is smaller than 0.37 eV for Cu_3N (100), but the hydrogenation of *CHO to CH_4 is always downhill on the Cu surface. The free energy of C-C coupling on Cu-C_3N_4 interface is even higher than that on Cu (111) surface, which is regarded as a catalyst for CH_4 generation [63,64]. Therefore, the hydrogenation of *CHO to CH_4 is prior on Cu-C_3N_4 surface. The Cu_3N (100) maintains a slightly higher Gibbs free energy for the *CO hydrogenation than Cu-C_3N_4, but the much lower free energy for C-C coupling will favor the C_2H_4 formation in competing with CH_4 path. The calculation results indicate that the tri-s-triazine structures are able to dramatically reduce the barrier for *CO hydrogenation to *CHO, and maintain a higher barrier for C-C coupling on Cu surface. Therefore, CuNCN-500 and CuNCN-600 show excellent CH_4 selectivity in both alkaline electrolyte and neutral electrolyte. The lower Gibbs free energy for *CHO formation and C-C coupling procedure on Cu_3N (100) surface and the higher CO content might be the reasons for the highest C_2H_4 Faradaic efficiency over CuNCN-300 catalyst.

4. Conclusions

In summary, we have proposed a facile strategy to prepare Cu-based/CxNy catalysts toward hydrocarbons via the pyrolysis of CuNCN at different temperatures. Through controllable manipulation of Cu states and the synergistic effect between g-C_3N_4 and Cu^+ species or Cu NPs, CuNCN-300 and CuNCN-x (x = 400, 500 and 600) achieve high Faradaic efficiency to C_2H_4 and CH_4, respectively. DFT calculations reveal that the Cu_3N in CuNCN-300 exhibits lower free energy for *CHO formation and C-C coupling procedure, resulting in a C_2H_4 Faradaic efficiency as high as 48.5% at 500 mA cm^{-2} with 1 M KOH as electrolyte. However, increasing the pyrolysis temperature above 400 °C, the tri-s-

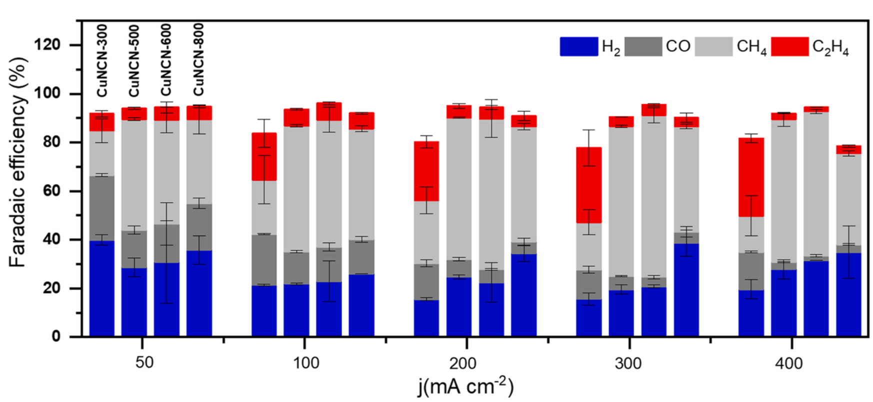

Fig. 5. Faradaic efficiencies of gaseous products for CuNCN-x (x = 300, 500, 600 and 800) in a flow cell with 1 M $KHCO_3$ as electrolyte.

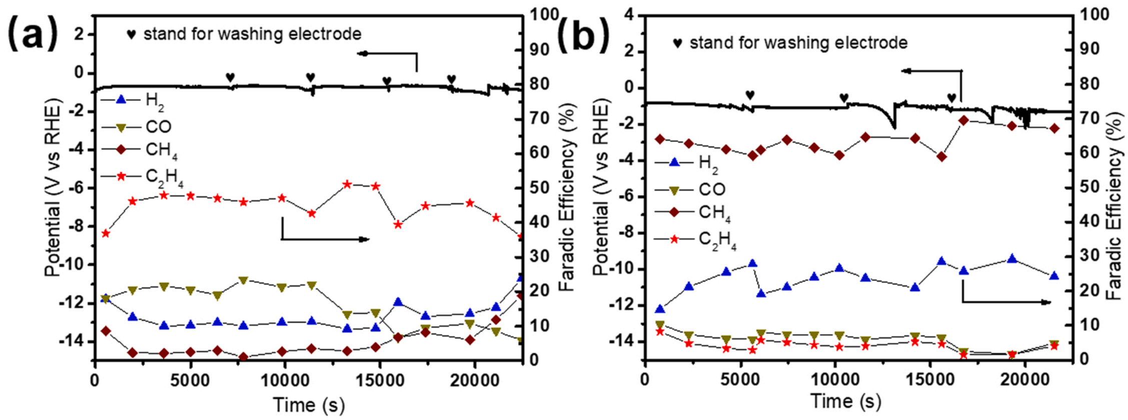

Fig. 6. Stability experiments for (a) CuNCN-300 at 500 mA cm^{-2} and (b) CuNCN-500 at 300 mA cm^{-2} in flow-cell with 1 M KOH as electrolyte.

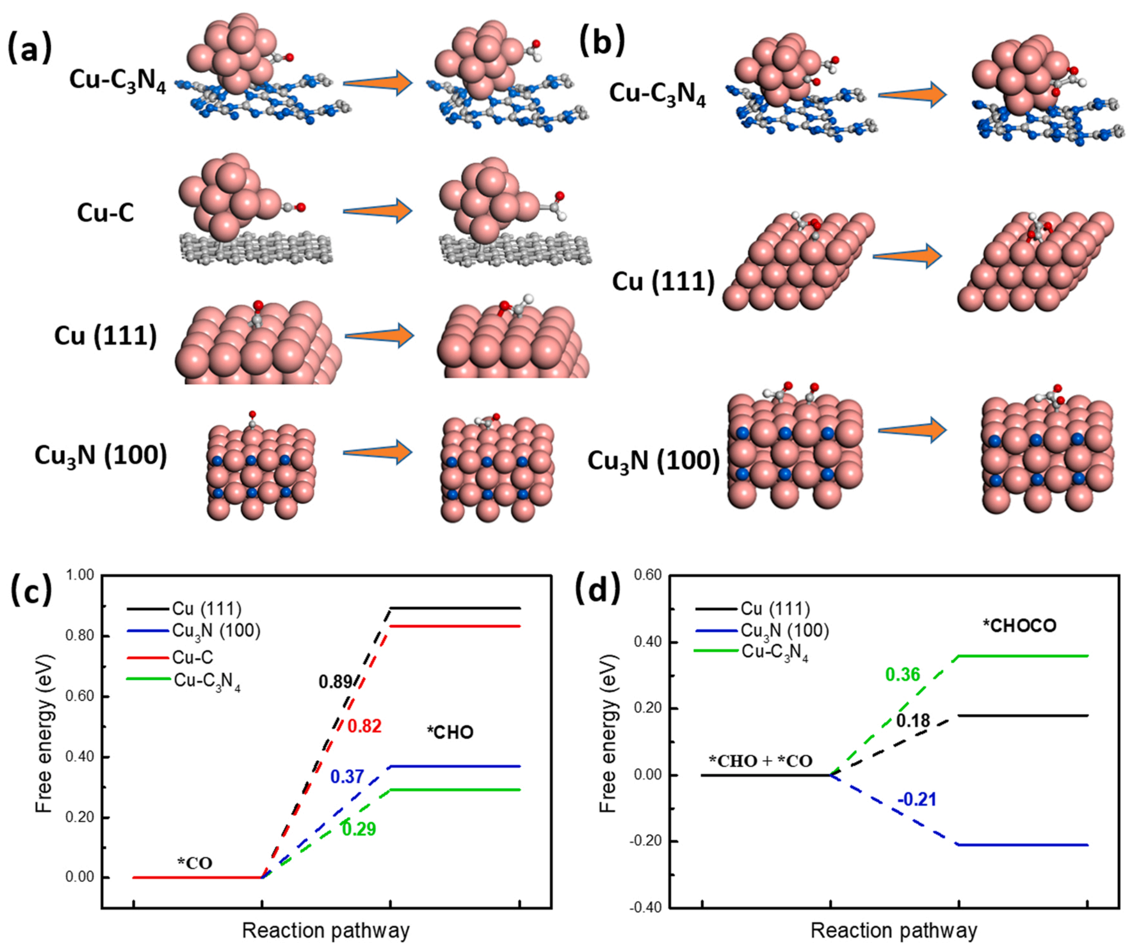

Fig. 7. (a) Adsorption configurations of *CO and *CHO on Cu-C_3N_4, Cu-C, Cu (111) and Cu_3N (100). (b) adsorption configurations of *CHO + *CO and *CHOCO on Cu-C_3N_4, Cu (111) and Cu_3N (100). (c) The free-energy diagram of *CO hydrogenation to *CHO on Cu (111), Cu_3N (100), Cu-C and Cu-C_3N_4. (d) *CHO coupling with *CO to *CHOCO on Cu (111), Cu_3N (100) and Cu-C_3N_4.

triazine structures in CxNy reduce the barrier for *CO hydrogenation and maintain higher free energy of 0.36 eV for *CHO-*CO coupling on Cu surface. Thus, CuNCN-500 and CuNCN-600 demonstrate high CH_4 Faradaic efficiency of 66.3% and 66.3% at 300 mA cm^{-2} with 1 M KOH, respectively. CuNCN-500 and CuNCN-600 could also achieve CH_4 selectivity of 66.2% and 68.7% with 1 M $KHCO_3$, showing superior resistance to the pH change of electrolyte. These results are expected to have a broad implication for the design of efficient electrocatalysts and an in-depth understanding of the synergistic effect between g-C_3N_4 and Cu^+ species or metallic Cu.

CRediT authorship contribution statement

Honglin Li: Conceptualization, Experiments, Visualization, Writing – original draft. **Shoufu Cao:** DFT calculations, Writing – original draft. **Hongman Sun:** Formal analysis, Writing – review & editing. **Yonglian Lu:** experiments, Formal analysis. **Xiaoqing Lu:** Writing – review & editing. **Jingbin Zeng:** Conceptualization, Writing – review & editing,

Supervision. **Zifeng Yan:** Conceptualization, Writing – review & editing, Supervision.

Declaration of Competing Interest

The authors declare that they have no known competing financial interests or personal relationships that could have appeared to influence the work reported in this paper.

Data Availability

Data will be made available on request.

Acknowledgements

This work was supported by the Key Projects of China National Key R&D Plan (2018YFE0118200), the Key Projects of Shandong Key R&D plan (2019JZZY010506), the Taishan Scholar Foundation (tspd20210308), the "111" Program of National College Disciplinary Innovation (B13031), the Innovation Project for Postgraduates of China University of Petroleum (East China) (YCX2020048), the National Natural Science Foundation of China (22102215), and the Fundamental Research Funds for the Central Universities (20CX02214A).

Appendix A. Supporting information

Supplementary data associated with this article can be found in the online version at doi:10.1016/j.apcatb.2022.121948.

References

[1] X. Zhang, J. Li, Y.Y. Li, Y. Jung, Y. Kuang, G. Zhu, Y. Liang, H. Dai, Selective and high current CO_2 electro-reduction to multicarbon products in near-neutral KCl electrolytes, J. Am. Chem. Soc. 143 (2021) 3245–3255, https://doi.org/10.1021/jacs.0c13427.
[2] G.M. Tomboc, S. Choi, T. Kwon, Y.J. Hwang, K. Lee, Potential link between Cu surface and selective CO_2 electroreduction: perspective on future electrocatalyst designs, Adv. Mater. 32 (2020), 1908398.
[3] J.B. Greenblatt, D.J. Miller, J.W. Ager, F.A. Houle, I.D. Sharp, The technical and energetic challenges of separating (photo)electrochemical carbon dioxide reduction products, Joule 2 (2018) 381–420, https://doi.org/10.1016/j.joule.2018.01.014.
[4] T.N. Nguyen, M. Salehi, Q.V. Le, A. Seifitokaldani, C.T. Dinh, Fundamentals of electrochemical CO_2 reduction on single-metal-atom catalysts, ACS Catal. 10 (2020) 10068–10095, https://doi.org/10.1021/acscatal.0c02643.
[5] L. Zhang, Z.J. Zhao, J. Gong, Nanostructured materials for heterogeneous electrocatalytic CO_2 reduction and their related reaction mechanisms, Angew. Chem. Int. Ed. 56 (2017) 11326–11353.
[6] Y. Zheng, A. Vasileff, X. Zhou, Y. Jiao, M. Jaroniec, S.-Z. Qiao, Understanding the roadmap for electrochemical reduction of CO_2 to multi-carbon oxygenates and hydrocarbons on copper-based catalysts, J. Am. Chem. Soc. 141 (2019) 7646–7659, https://doi.org/10.1021/jacs.9b02124.
[7] A. Bagger, W. Ju, A.S. Varela, P. Strasser, J. Rossmeisl, Electrochemical CO_2 reduction: a classification problem, Chemphyschem 18 (2017) 3266–3273, https://doi.org/10.1002/cphc.201700736.
[8] R. Daiyan, W.H. Saputera, H. Masood, J. Leverett, X. Lu, R. Amal, A disquisition on the active sites of heterogeneous catalysts for electrochemical reduction of CO_2 to value-added chemicals and fuel, Adv. Energy Mater. 10 (2020), 1902106.
[9] Z.-Z. Wu, F.-Y. Gao, M.-R. Gao, Regulating the oxidation state of nanomaterials for electrocatalytic CO_2 reduction, Energy Environ. Sci. 14 (2021) 1121–1139, https://doi.org/10.1039/D0EE02747B.
[10] T. Zhang, W. Li, K. Huang, H. Guo, Z. Li, Y. Fang, R.M. Yadav, V. Shanov, P. M. Ajayan, L. Wang, C. Lian, J. Wu, Regulation of functional groups on graphene quantum dots directs selective CO_2 to CH_4 conversion, Nat. Commun. 12 (2021) 5265, https://doi.org/10.1038/s41467-021-25640-1.
[11] J. Gao, H. Zhang, X. Guo, J. Luo, S.M. Zakeeruddin, D. Ren, M. Grätzel, Selective C–C coupling in carbon dioxide electroreduction via efficient spillover of intermediates as supported by operando raman spectroscopy, J. Am. Chem. Soc. 141 (2019) 18704–18714, https://doi.org/10.1021/jacs.9b07415.
[12] T.T.H. Hoang, S. Verma, S. Ma, T.T. Fister, J. Timoshenko, A.I. Frenkel, P.J. A. Kenis, A.A. Gewirth, Nanoporous copper–silver alloys by additive-controlled electrodeposition for the selective electroreduction of CO_2 to ethylene and ethanol, J. Am. Chem. Soc. 140 (2018) 5791–5797, https://doi.org/10.1021/jacs.8b01868.
[13] Y.C. Li, Z. Wang, T. Yuan, D.-H. Nam, M. Luo, J. Wicks, B. Chen, J. Li, F. Li, F.P. G. de Arquer, Y. Wang, C.-T. Dinh, O. Voznyy, D. Sinton, E.H. Sargent, Binding site diversity promotes CO_2 electroreduction to ethanol, J. Am. Chem. Soc. 141 (2019) 8584–8591, https://doi.org/10.1021/jacs.9b02945.
[14] Y. Li, A. Xu, Y. Lum, X. Wang, S.-F. Hung, B. Chen, Z. Wang, Y. Xu, F. Li, J. Abed, J. E. Huang, A.S. Rasouli, J. Wicks, L.K. Sagar, T. Peng, A.H. Ip, D. Sinton, H. Jiang, C. Li, E.H. Sargent, Promoting CO_2 methanation via ligand-stabilized metal oxide clusters as hydrogen-donating motifs, Nat. Commun. 11 (2020) 6190, https://doi.org/10.1038/s41467-020-20004-7.
[15] X. Wei, Z. Yin, K. Lyu, Z. Li, J. Gong, G. Wang, L. Xiao, J. Lu, L. Zhuang, Highly selective reduction of CO_2 to C_{2+} hydrocarbons at copper/polyaniline interfaces, ACS Catal. 10 (2020) 4103–4111, https://doi.org/10.1021/acscatal.0c00049.
[16] M.S. Xie, B.Y. Xia, Y. Li, Y. Yan, Y. Yang, Q. Sun, S.H. Chan, A. Fisher, X. Wang, Amino acid modified copper electrodes for the enhanced selective electroreduction of carbon dioxide towards hydrocarbons, Energy Environ. Sci. 9 (2016) 1687–1695, https://doi.org/10.1039/C5EE03694A.
[17] F. Li, A. Thevenon, A. Rosas-Hernández, Z. Wang, Y. Li, C.M. Gabardo, A. Ozden, C. T. Dinh, J. Li, Y. Wang, J.P. Edwards, Y. Xu, C. McCallum, L. Tao, Z.-Q. Liang, M. Luo, X. Wang, H. Li, C.P. O'Brien, C.-S. Tan, D.-H. Nam, R. Quintero-Bermudez, T.-T. Zhuang, Y.C. Li, Z. Han, R.D. Britt, D. Sinton, T. Agapie, J.C. Peters, E. H. Sargent, Molecular tuning of CO_2-to-ethylene conversion, Nature 577 (2020) 509–513, https://doi.org/10.1038/s41586-019-1782-2.
[18] X. Chen, J. Chen, N.M. Alghoraibi, D.A. Henckel, R. Zhang, U.O. Nwabara, K. E. Madsen, P.J.A. Kenis, S.C. Zimmerman, A.A. Gewirth, Electrochemical CO_2-to-ethylene conversion on polyamine-incorporated Cu electrodes, Nat. Catal. 4 (2020) 20–27, https://doi.org/10.1038/s41929-020-00547-0.
[19] Z. Li, Y. Yang, Z. Yin, X. Wei, H. Peng, K. Lyu, F. Wei, L. Xiao, G. Wang, H. D. Abruña, J. Lu, L. Zhuang, Interface-enhanced catalytic selectivity on the C_2 products of CO_2 electroreduction, ACS Catal. 11 (2021) 2473–2482, https://doi.org/10.1021/acscatal.0c03846.
[20] Z. Yin, C. Yu, Z. Zhao, X. Guo, M. Shen, N. Li, M. Muzzio, J. Li, H. Liu, H. Lin, J. Yin, G. Lu, D. Su, S. Sun, Cu3N nanocubes for selective electrochemical reduction of CO_2 to ethylene, Nano Lett. 19 (2019) 8658–8663, https://doi.org/10.1021/acs.nanolett.9b03324.
[21] C. Zhao, G. Luo, X. Liu, W. Zhang, Z. Li, Q. Xu, Q. Zhang, H. Wang, D. Li, F. Zhou, In situ topotactic transformation of an interstitial alloy for CO electroreduction, Adv. Mater. 32 (2020), 2002382.
[22] C. Peng, G. Luo, Z. Xu, S. Yan, J. Zhang, M. Chen, L. Qian, W. Wei, Q. Han, G. Zheng, Lithiation-enabled high-density nitrogen vacancies electrocatalyze CO_2 to C_2 products, Adv. Mater. 33 (2021), 2103150.
[23] D. Gao, T. Liu, G. Wang, X. Bao, Structure sensitivity in single-atom catalysis toward CO_2 electroreduction, ACS Energy Lett. 6 (2021) 713–727, https://doi.org/10.1021/acsenergylett.0c02665.
[24] J. Kim, W. Choi, J.W. Park, C. Kim, M. Kim, H. Song, Branched copper oxide nanoparticles induce highly selective ethylene production by electrochemical carbon dioxide reduction, J. Am. Chem. Soc. 141 (2019) 6986–6994, https://doi.org/10.1021/jacs.9b00911.
[25] Q. Li, W. Zhu, J. Fu, H. Zhang, G. Wu, S. Sun, Controlled assembly of Cu nanoparticles on pyridinic-N rich graphene for electrochemical reduction of CO_2 to ethylene, Nano Energy 24 (2016) 1–9, https://doi.org/10.1016/j.nanoen.2016.03.024.
[26] J. Zhang, Y. Guo, B. Shang, T. Fan, X. Lian, P. Huang, Y. Dong, Z. Chen, X. Yi, Unveiling the synergistic effect between graphitic carbon nitride and Cu_2O toward CO_2 electroreduction to C_2H_4, ChemSusChem 14 (2021) 929–937, https://doi.org/10.1002/cssc.202002427.
[27] W. Lin, H. Chen, Z. Li, K. Sasaki, S. Yao, Z. Zhang, J. Li, J. Fu, A Cu_2O-derived polymeric carbon nitride heterostructured catalyst for the electrochemical reduction of carbon dioxide to ethylene, ChemSusChem 14 (2021) 3190–3197, https://doi.org/10.1002/cssc.202100659.
[28] Y. Pan, H. Li, J. Xiong, Y. Yu, H. Du, S. Li, Z. Wu, S. Li, J. Lai, L. Wang, Protecting the state of Cu clusters and nanoconfinement engineering over hollow mesoporous carbon spheres for electrocatalytical C-C coupling, Appl. Catal. B 306 (2022), 121111, https://doi.org/10.1016/j.apcatb.2022.121111.
[29] Y. Geng, D. Chen, N. Li, Q. Xu, H. Li, J. He, J. Lu, Z-Scheme 2D/2D α-Fe_2O_3/g-C_3N_4 heterojunction for photocatalytic oxidation of nitric oxide, Appl. Catal. B 280 (2021), 119409, https://doi.org/10.1016/j.apcatb.2020.119409.
[30] S. Zhao, Z. Tang, S. Guo, M. Han, C. Zhu, Y. Zhou, L. Bai, J. Gao, H. Huang, Y. Li, Y. Liu, Z. Kang, Enhanced activity for CO_2 electroreduction on a highly active and stable ternary Au-CDots-C_3N_4 electrocatalyst, ACS Catal. 8 (2018) 188–197, https://doi.org/10.1021/acscatal.7b01551.
[31] G.W. Woyessa, J.-aB. dela Cruz, M. Rameez, C.-H. Hung, Nanocomposite catalyst of graphitic carbon nitride and Cu/Fe mixed metal oxide for electrochemical CO_2 reduction to CO, Appl. Catal. B 291 (2021), 120052, https://doi.org/10.1016/j.apcatb.2021.120052.
[32] L. Zhang, F. Mao, L.R. Zheng, H.F. Wang, X.H. Yang, H.G. Yang, Tuning metal catalyst with metal–C3N4 interaction for efficient CO_2 electroreduction, ACS Catal. 8 (2018) 11035–11041, https://doi.org/10.1021/acscatal.8b03789.
[33] Y. Jiao, Y. Zheng, P. Chen, M. Jaroniec, S.Z. Qiao, Molecular scaffolding strategy with synergistic active centers to facilitate electrocatalytic CO_2 reduction to hydrocarbon/alcohol, J. Am. Chem. Soc. 139 (2017) 18093–18100, https://doi.org/10.1021/jacs.7b10817.
[34] S. Fu, X. Liu, J. Ran, Y. Jiao, S.-Z. Qiao, CO_2 reduction by single copper atom supported on g-C3N4 with asymmetrical active sites, Appl. Surf. Sci. 540 (2021), 148293, https://doi.org/10.1016/j.apsusc.2020.148293.
[35] P.P. Yang, X.L. Zhang, F.Y. Gao, Y.R. Zheng, Z.Z. Niu, X. Yu, R. Liu, Z.Z. Wu, S. Qin, L.P. Chi, Y. Duan, T. Ma, X.S. Zheng, J.F. Zhu, H.J. Wang, M.R. Gao, S.H. Yu, Protecting copper oxidation state via intermediate confinement for selective CO_2 electroreduction to C_{2+} fuels, J. Am. Chem. Soc. 142 (2020) 6400–6408, https://doi.org/10.1021/jacs.0c01699.

[36] P. De Luna, R. Quintero-Bermudez, C.-T. Dinh, M.B. Ross, O.S. Bushuyev, P. Todorović, T. Regier, S.O. Kelley, P. Yang, E.H. Sargent, Catalyst electro-redeposition controls morphology and oxidation state for selective carbon dioxide reduction, Nat. Catal. 1 (2018) 103–110, https://doi.org/10.1038/s41929-017-0018-9.
[37] Q. Fan, X. Zhang, X. Ge, L. Bai, D. He, Y. Qu, C. Kong, J. Bi, D. Ding, Y. Cao, X. Duan, J. Wang, J. Yang, Y. Wu, Manipulating Cu nanoparticle surface oxidation states tunes catalytic selectivity toward CH_4 or C_{2+} products in CO_2 electroreduction, Adv. Energy Mater. 11 (2021), 2101424, https://doi.org/10.1002/aenm.202101424.
[38] J. Xu, F. Xu, M. Qian, Z. Li, P. Sun, Z. Hong, F. Huang, Copper nanodot-embedded graphene urchins of nearly full-spectrum solar absorption and extraordinary solar desalination, Nano Energy 53 (2018) 425–431, https://doi.org/10.1016/j.nanoen.2018.08.067.
[39] X. Xu, H. Zeng, D. Han, K. Qiao, W. Xing, M.J. Rood, Z. Yan, Nitrogen and sulfur co-doped graphene nanosheets to improve anode materials for sodium-ion batteries, ACS Appl. Mater. Interfaces 10 (2018) 37172–37180, https://doi.org/10.1021/acsami.8b15940.
[40] T. Zhang, T. Cai, W. Xing, T. Li, B. Liang, H. Hu, L. Zhao, X. Li, Z. Yan, A rechargeable 6-electron Al–Se battery with high energy density, Energy Storage Mater. 41 (2021) 667–676, https://doi.org/10.1016/j.ensm.2021.06.041.
[41] G. Kresse, J. Furthmüller, Efficient iterative schemes for ab initio total-energy calculations using a plane-wave basis set, Phys. Rev. B 54 (1996) 11169–11186.
[42] J.P. Perdew, K. Burke, M. Ernzerhof, Generalized gradient approximation made simple, Phys. Rev. Lett. 77 (1996) 3865–3868.
[43] K. Mathew, R. Sundararaman, K. Letchworth-Weaver, T.A. Arias, R.G. Hennig, Implicit solvation model for density-functional study of nanocrystal surfaces and reaction pathways, J. Chem. Phys. 140 (2014), 084106.
[44] J.K. N?Rskov, J. Rossmeisl, A. Logadottir, L. Lindqvist, J.R. Kitchin, T. Bligaard, H. Jónsson, Origin of the overpotential for oxygen reduction at a fuel-cell cathode, J. Phys. Chem. B 108 (2004) 17886–17892.
[45] A. Jain, S.P. Ong, G. Hautier, W. Chen, W.D. Richards, S. Dacek, S. Cholia, D. Gunter, D. Skinner, G. Ceder, Commentary: the materials project: a materials genome approach to accelerating materials innovation, APL Mater. 1 (2013), 011002.
[46] Z. Chen, P. Sun, B. Fan, Z. Zhang, X. Fang, In situ template-free ion-exchange process to prepare visible-light-Active g-C_3N_4/NiS hybrid photocatalysts with enhanced hydrogen evolution activity, J. Phys. Chem. C 118 (2014) 7801–7807, https://doi.org/10.1021/jp5000232.
[47] T. Li, L. Zhao, Y. He, J. Cai, M. Luo, J. Lin, Synthesis of g-C_3N_4/$SmVO_4$ composite photocatalyst with improved visible light photocatalytic activities in RhB degradation, Appl. Catal. B 129 (2013) 255–263, https://doi.org/10.1016/j.apcatb.2012.09.031.
[48] A. Eguía-Barrio, E. Castillo-Martínez, X. Liu, R. Dronskowski, M. Armand, T. Rojo, Carbodiimides: new materials applied as anode electrodes for sodium and lithium ion batteries, J. Mater. Chem. A 4 (2016) 1608–1611, https://doi.org/10.1039/C5TA08945J.
[49] C. Wu, S. Xue, Z. Qin, M. Nazari, G. Yang, S. Yue, T. Tong, H. Ghasemi, F.C. R. Hernandez, S. Xue, D. Zhang, H. Wang, Z.M. Wang, S. Pu, J. Bao, Making g-C_3N_4 ultra-thin nanosheets active for photocatalytic overall water splitting, Appl. Catal. B 282 (2021), 119557, https://doi.org/10.1016/j.apcatb.2020.119557.
[50] D. Ressnig, G. Clavel, N. Scharnagl, M. Antonietti, Dye-mediated growth of 2D coppercarbodiimide (CuNCN) nanostructures and their metamorphosis into a 3D Cu@ CxNy Hybrid, Part. Part. Syst. Char. 31 (2014) 557–560.
[51] Q. Han, B. Wang, Y. Zhao, C. Hu, L. Qu, A graphitic-C_3N_4 "seaweed" architecture for enhanced hydrogen evolution, Angew. Chem. Int. Ed. 54 (2015) 11433–11437.
[52] B. Jürgens, E. Irran, J. Senker, P. Kroll, H. Müller, W. Schnick, Melem (2,5,8-Triamino-tri-s-triazine), an important intermediate during condensation of melamine rings to graphitic carbon nitride: synthesis, structure determination by X-ray powder diffractometry, solid-state NMR, and theoretical studies, J. Am. Chem. Soc. 125 (2003) 10288–10300, https://doi.org/10.1021/ja0357689.
[53] Z. Zhang, K. Leinenweber, M. Bauer, L.A.J. Garvie, P.F. McMillan, G.H. Wolf, High-pressure bulk synthesis of crystalline $C_6N_9H_3 \cdot HCl$: a novel C_3N_4 graphitic derivative, J. Am. Chem. Soc. 123 (2001) 7788–7796, https://doi.org/10.1021/ja0103849.
[54] H. Yu, R. Shi, Y. Zhao, T. Bian, Y. Zhao, C. Zhou, G.I. Waterhouse, L.Z. Wu, C. H. Tung, T. Zhang, Alkali-assisted synthesis of nitrogen deficient graphitic carbon nitride with tunable band structures for efficient visible-light-driven hydrogen evolution, Adv. Mater. 29 (2017), 1605148.
[55] Y. Qin, J. Yuan, J. Li, D. Chen, Y. Kong, F. Chu, Y. Tao, M. Liu, Crosslinking graphene oxide into robust 3D porous N-doped graphene, Adv. Mater. 27 (2015) 5171–5175.
[56] D. Wei, Y. Liu, Y. Wang, H. Zhang, L. Huang, G. Yu, Synthesis of N-doped graphene by chemical vapor deposition and its electrical properties, Nano Lett. 9 (2009) 1752–1758, https://doi.org/10.1021/nl803279t.
[57] B. Wang, L. Si, J. Geng, Y. Su, Y. Li, X. Yan, L. Chen, Controllable magnetic 3D nitrogen-doped graphene gel: Synthesis, characterization, and catalytic performance, Appl. Catal. B 204 (2017) 316–323, https://doi.org/10.1016/j.apcatb.2016.11.042.
[58] L. Wang, Z. Sofer, J. Luxa, M. Pumera, Nitrogen doped graphene: influence of precursors and conditions of the synthesis, J. Mater. Chem. C. 2 (2014) 2887–2893, https://doi.org/10.1039/C3TC32359E.
[59] K. Sato, R. Saito, Y. Oyama, J. Jiang, L. Cancado, M. Pimenta, A. Jorio, G. G. Samsonidze, G. Dresselhaus, M. Dresselhaus, D-band Raman intensity of graphitic materials as a function of laser energy and crystallite size, Chem. Phys. Lett. 427 (2006) 117–121.
[60] H. Wang, T. Maiyalagan, X. Wang, Review on recent progress in nitrogen-doped graphene: synthesis, characterization, and its potential applications, ACS Catal. 2 (2012) 781–794, https://doi.org/10.1021/cs200652y.
[61] B. You, L. Wang, L. Yao, J. Yang, Three dimensional N-doped graphene–CNT networks for supercapacitor, Chem. Commun. 49 (2013) 5016–5018, https://doi.org/10.1039/C3CC41949E.
[62] D.M. Weekes, D.A. Salvatore, A. Reyes, A. Huang, C.P. Berlinguette, Electrolytic CO_2 reduction in a flow cell, Acc. Chem. Res. 51 (2018) 910–918, https://doi.org/10.1021/acs.accounts.8b00010.
[63] H. Dong, Y. Li, D.-e Jiang, First-principles insight into electrocatalytic reduction of CO_2 to CH_4 on a copper nanoparticle, J. Phys. Chem. C. 122 (2018) 11392–11398, https://doi.org/10.1021/acs.jpcc.8b01928.
[64] G.L. De Gregorio, T. Burdyny, A. Loiudice, P. Iyengar, W.A. Smith, R. Buonsanti, Facet-dependent selectivity of Cu catalysts in electrochemical CO_2 reduction at commercially viable current densities, ACS Catal. 10 (2020) 4854–4862, https://doi.org/10.1021/acscatal.0c00297.